Available online at www.sciencedirect.com
SCIENCE DIRECT®
Journal of Sound and Vibration 276 (2004) 571–592
JOURNAL OF SOUND AND VIBRATION
www.elsevier.com/locate/jsvi

Equivalent acoustic impedance model. Part 1: experiments and semi-physical model

B. Faverjon, C. Soize*

Laboratoire de Mécanique, Université de Marne-La-Vallée, 5 boulevard Descartes, 77454 Marne-La-Vallée Cedex 02, France

Received 10 February 2003; accepted 4 August 2003

Abstract

The context of this research is devoted to the construction of an equivalent acoustic impedance model for a soundproofing scheme consisting of a three-dimensional porous medium inserted between two thin plates. Part 1 of this paper presents the experiments performed and a probabilistic algebraic model of the wall acoustic impedance constructed using the experimental data basis for the medium- and high-frequency ranges. The probabilistic algebraic model is constructed by using the general mathematical properties of wall acoustic impedance operators (symmetry, odd and even functions with respect to the frequency, decreasing functions when frequency goes to infinity, behaviour when frequency goes to zero and so on). The parameters introduced in this probabilistic algebraic model are fitted with the experimental data basis. Finally, this probabilistic algebraic model summarizes all the experimental data bases and consequently can be reused for other researches.

1. Introduction

In the medium- and high-frequency ranges, the modelling of a multilayer system containing porous materials is very important for noise control in aircrafts, automobiles, buildings, etc. Difficulties occur in modelling such multilayer systems and in validating them with experimental data bases. Many works have already been published about experimental data bases concerning the acoustic transmission through multilayer systems or concerning the surface impedance of multilayer systems with a rigid wall [1–10]. Nevertheless, very little information exists concerning the experimental data basis for the equivalent acoustic impedance of multilayer systems with porous media and for the medium- and high-frequency ranges. Such experimental data bases are necessary to understand the

*Corresponding author. Tel.: +33-1-60-95-77-91; fax: +33-1-60-95-77-99.
E-mail address: soize@univ-mlv.fr (C. Soize).

0022-460X/$ - see front matter
doi:10.1016/j.jsv.2003.08.053

physics of such systems and to validate analytical and numerical models in the medium- and high-frequency ranges. The main objective of Part 1 of this paper is to present an experimental data basis concerning the equivalent acoustic impedance of a multilayer system containing a porous medium and to propose a probabilistic model which allows the experimental data basis to be synthesized and consequently, to be reused by the community for other researches. In particular, this experimental data bases will be used in Part 2 [11] of this paper which is devoted to the validation of an analytical model of such a multilayer system for the medium- and high-frequency ranges. The experimental multilayer system consists of a three-dimensional porous medium inserted between two thin plates. At a given frequency, the equivalent acoustic impedance of such a multilayer system is the linear mapping between the pressure field applied to one plate and the jump of the normal velocities to each plate. Such an equivalent acoustic impedance can be introduced in the models allowing vibro-acoustic predictions of complex mechanical systems. An experimental data basis has specifically been constructed for this research [12] and corresponds to the experimental identification of the equivalent acoustic impedance in the frequency band [100,1600] Hz, the medium and high ranges corresponding to the frequency band [300,1600] Hz. Using this experimental data basis, a probabilistic algebraic model of the equivalent acoustic impedance of the multilayer system is constructed. This probabilistic model synthesizes all the experimental data bases through the use of a mean algebraic model and a random fluctuation model [13,14]. The number of parameters of this model (correlation lengths) is minimum. A good approximation of this experimental data basis is given by this model. Section 2 deals with the experiment. In Section 3, the construction of the basic algebraic model for the equivalent acoustic impedance is developed. Section 4 is devoted to the properties of the equivalent acoustic impedance which are deduced from the analysis of the experimental data basis. In Section 5, one presents the estimation of the mean values of the basic algebraic model parameters using the experimental data basis and finally, Section 6 deals with the construction of the random model.

2. Description of an equivalent acoustic impedance experiment

An experiment [12] was carried out in an anechoic room in order to measure the equivalent acoustic impedance of a multilayer system consisting of a three-dimensional porous medium inserted between two thin plates in aluminium, denoted as P_1 and P_2 (see Fig. 1). The length and width of the multilayer system are 0.6 and 0.4 m respectively. This multilayer system is fixed in a rigid baffle. The geometry and the material properties of the experimental multilayer system are described in Appendix A. The experimental analysis and the signal processing are performed in the frequency domain. The angular frequency is denoted by ω. Normal point forces to plate P_1 are successively applied to the $N = 25$ points $M_1, \ldots, M_N$ defined in Fig. 2. The normal velocities at

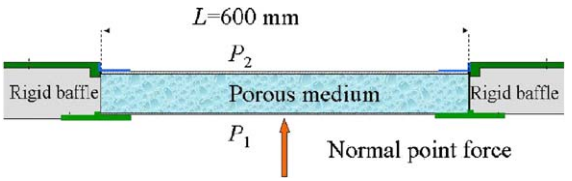

Fig. 1. Description of the experiment.

these N driving points are measured using laser velocimetry (see Fig. 3). Consequently, the N points $M_1, \ldots, M_N$ in plate P_1 are driving and receiving points. In addition, the normal accelerations are measured at N points $\tilde{M}_1, \ldots, \tilde{M}_N$ in plate P_2 (see Fig. 4) and then, the associated normal velocities are deduced on plate P_2. These N receiving points $\tilde{M}_1, \ldots, \tilde{M}_N$ in plate P_2 correspond to the N points $M_1, \ldots, M_N$ in plate P_1 which means that, for all $j = 1, \ldots, N$, point M_j and point $\tilde{M}_j$ have the same co-ordinates x_1 and x_2 (but have a different co-ordinate x_3). This choice allows the jump of the normal velocities between the two sides of the multilayer system to be calculated. Let $F_k^{exp}(\omega)$ be the normal point force applied to point M_k belonging to the N driving points $M_1, \ldots, M_N$ in plate P_1. Excitation $F_k^{exp}(\omega)$ induces the normal velocities $V_{jk}^{P_1\,exp}(\omega)$ and $V_{jk}^{P_2\,exp}(\omega)$ at receiving point M_j in plate P_1 and at corresponding receiving point $\tilde{M}_j$ in plate P_2, respectively. Let $\Delta\mathbf{V}^{exp}(\omega) = (\Delta V_{1k}^{exp}(\omega), \ldots, \Delta V_{Nk}^{exp}(\omega))$ with $\Delta V_{jk}^{exp}(\omega) = V_{jk}^{P_1\,exp}(\omega) - V_{jk}^{P_2\,exp}(\omega)$ be the jump of the normal velocities to the N couples of points $(M_j, \tilde{M}_j)$. For each k fixed in $\{1, \ldots, 25\}$ and for 8192 values of ω in the frequency band of analysis [30,1600] Hz, the experimental measures allow the $(N \times N)$ complex matrix-valued frequency response function $[\mathbf{H}^{exp}(\omega)]$ to be constructed for a linear filter whose inputs are the normal forces applied to N nodes of plate P_1 and whose outputs are the jump of the normal velocities at the N couples of points $(M_j, \tilde{M}_j)$. Consequently, one has

$$\Delta\mathbf{V}^{exp}(\omega) = [\mathbf{H}^{exp}(\omega)]\,\mathbf{F}^{exp}(\omega) \quad \text{in which } [\mathbf{H}^{exp}(\omega)] = \begin{bmatrix} \Delta V_{11}^{exp}(\omega) & \cdots & \Delta V_{1N}^{exp}(\omega) \\ \vdots & & \\ \Delta V_{N1}^{exp}(\omega) & \cdots & \Delta V_{NN}^{exp}(\omega) \end{bmatrix},$$

$$\mathbf{F}^{exp}(\omega) = (F_1^{exp}(\omega), \ldots, F_N^{exp}(\omega)). \tag{1}$$

Let $\mathscr{B} = [100, 1600]$ Hz be the frequency band of analysis for which the experimental frequency response function $[\mathbf{H}^{exp}(\omega)]$ is invertible. For ω in $\mathscr{B}$, the experimental impedance $N \times N$ complex matrix $[\mathbf{Z}^{exp}(\omega)]$ is then defined by

$$[\mathbf{Z}^{exp}(\omega)] = [\mathbf{H}^{exp}(\omega)]^{-1}, \quad \forall\omega \in \mathscr{B}. \tag{2}$$

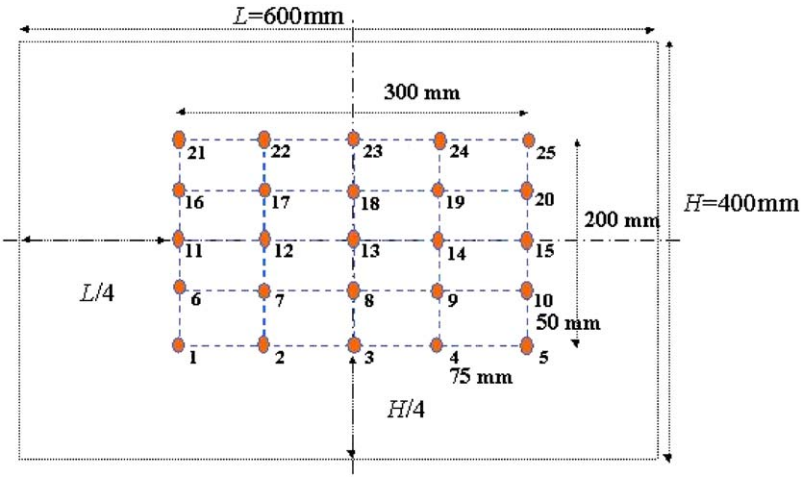

Fig. 2. Location of the 25 driving and receiving points in plate P_1.

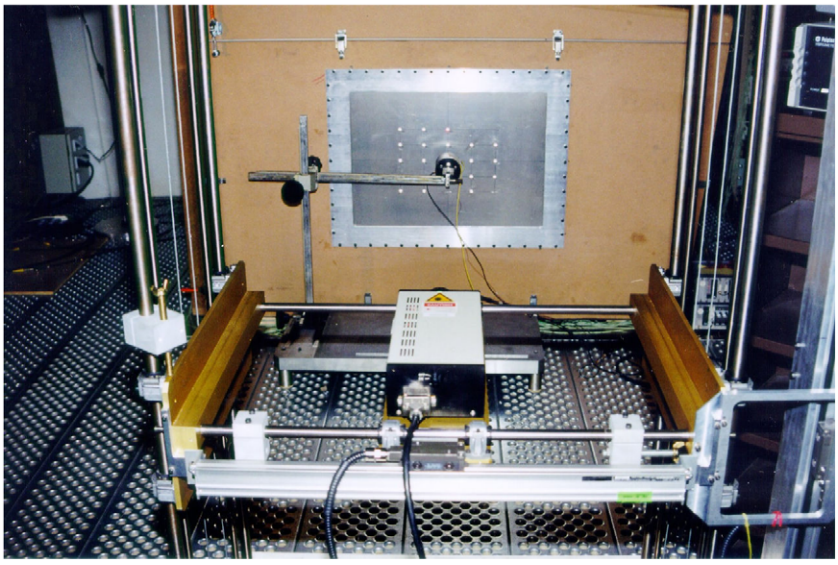

Fig. 3. For plate P_1, 25 driving points excited with a shaker and 25 receiving points measured using laser velocimetry.

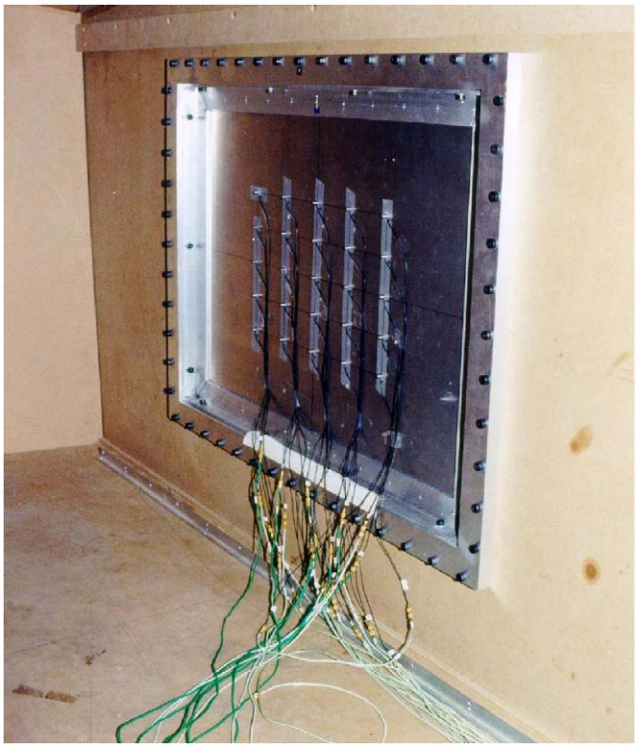

Fig. 4. For plate P_2, 25 receiving points measured by accelerometers.

3. Construction of the basic algebraic model for an equivalent acoustic impedance

3.1. Setting the problem

The geometry of the multilayer system is shown in Fig. 5. The interfaces between the porous medium and the plates P_1 and P_2 are denoted by Σ_1 and Σ_2. The theoretical model which is considered introduces an applied pressure field p acting on surface Σ_0. The reference-plane surface system of the multilayer system is denoted by S and coincides with surface Σ_1. The co-ordinates (x_1, x_2, x_3) of a point belonging to the porous medium are given in the cartesian system whose origin belongs to the reference-plane S. The x_3 co-ordinate of the coupling interface Σ_1 (or Σ_2) is 0 (or H) (in which H is the thickness of the porous medium). Below, $\tilde{\mathbf{x}} = (x_1, x_2)$ denotes the point belonging to reference plane S. Let S_1 and S_2 be the mid-planes of the plates P_1 and P_2.

3.2. Definition of the equivalent acoustic impedance density function

The experimental measures have been made in an anechoic room such that the effect of the coupling between the external air and the multilayer system can be considered as negligible compared to the effect of the viscous dissipation of the multilayer system. Let $v^{P_1}(\tilde{\mathbf{x}}, \omega)$ and $v^{P_2}(\tilde{\mathbf{x}}, \omega)$ be the normal velocities at the point M in plate P_1 and at the corresponding point $\tilde{M}$ in plate P_2 such that the corresponding points M and $\tilde{M}$ have the same co-ordinates $\tilde{\mathbf{x}} = (x_1, x_2)$. For fixed ω, the equivalent acoustic impedance is the integral operator $\mathbb{Z}(\omega)$ defined by a density function $z(\tilde{\mathbf{x}}, \tilde{\mathbf{x}}', \omega)$ with complex values such that

$$p(\tilde{\mathbf{x}}, \omega) = \{\mathbb{Z}(\omega)\,(v^{P_1}(\cdot, \omega) - v^{P_2}(\cdot, \omega))\}(\tilde{\mathbf{x}}) = \int_{\tilde{\mathbf{x}}' \in S} z(\tilde{\mathbf{x}}, \tilde{\mathbf{x}}', \omega)\,(v^{P_1}(\tilde{\mathbf{x}}', \omega) - v^{P_2}(\tilde{\mathbf{x}}', \omega))\,\mathrm{d}S_{\tilde{\mathbf{x}}'}, \tag{3}$$

in which $(\tilde{\mathbf{x}}, \tilde{\mathbf{x}}') \mapsto z(\tilde{\mathbf{x}}, \tilde{\mathbf{x}}', \omega)$ is called the equivalent acoustic impedance density function and where $\mathrm{d}S_{\tilde{\mathbf{x}}'} = \mathrm{d}\tilde{x}'_1\,\mathrm{d}\tilde{x}'_2$. It should be noted that the complex operator $\mathbb{Z}(\omega)$ is defined by the complex bilinear form

$$\langle\, \mathbb{Z}(\omega)\, u, v \,\rangle = \int_S \int_S z(\tilde{\mathbf{x}}, \tilde{\mathbf{x}}', \omega)\, u(\tilde{\mathbf{x}}')\, v(\tilde{\mathbf{x}})\, \mathrm{d}S_{\tilde{\mathbf{x}}}\, \mathrm{d}S_{\tilde{\mathbf{x}}'}. \tag{4}$$

It is assumed that the reciprocity principles can be applied. Therefore, the complex operator $\mathbb{Z}(\omega)$ is symmetric and consequently, $z(\tilde{\mathbf{x}}, \tilde{\mathbf{x}}', \omega)$ satisfies the following symmetry property:

$$z(\tilde{\mathbf{x}}, \tilde{\mathbf{x}}', \omega) = z(\tilde{\mathbf{x}}', \tilde{\mathbf{x}}, \omega). \tag{5}$$

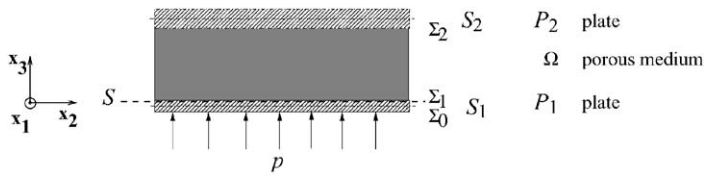

Fig. 5. Geometry of the multilayer system.

Moreover, the system being considered a physical system, we have the property that $\mathbb{Z}(-\omega) = \overline{\mathbb{Z}(\omega)}$ which yields

$$z(\tilde{\mathbf{x}}, \tilde{\mathbf{x}}', -\omega) = \overline{z(\tilde{\mathbf{x}}, \tilde{\mathbf{x}}', \omega)}, \tag{6}$$

where $\bar{a}$ denotes the conjugate of the complex number a. Introducing the real and the imaginary parts of the equivalent acoustic impedance density function such that $z(\tilde{\mathbf{x}}, \tilde{\mathbf{x}}', \omega) = z_R(\tilde{\mathbf{x}}, \tilde{\mathbf{x}}', \omega) + \mathrm{i} z_I(\tilde{\mathbf{x}}, \tilde{\mathbf{x}}', \omega)$, from Eqs. (5) and (6), it can be deduced that

$$z_R(\tilde{\mathbf{x}}, \tilde{\mathbf{x}}', \omega) = z_R(\tilde{\mathbf{x}}', \tilde{\mathbf{x}}, \omega), \quad z_I(\tilde{\mathbf{x}}, \tilde{\mathbf{x}}', \omega) = z_I(\tilde{\mathbf{x}}', \tilde{\mathbf{x}}, \omega), \tag{7}$$

$$z_R(\tilde{\mathbf{x}}, \tilde{\mathbf{x}}', -\omega) = z_R(\tilde{\mathbf{x}}, \tilde{\mathbf{x}}', \omega), \quad z_I(\tilde{\mathbf{x}}, \tilde{\mathbf{x}}', -\omega) = -z_I(\tilde{\mathbf{x}}, \tilde{\mathbf{x}}', \omega). \tag{8}$$

The correspondence between the continuous model defined by Eq. (3) and the discrete experimental model defined by Eq. (1) is obtained by discretizing Eq. (3) using the usual collocation method with the N points of the mesh.

3.3. Local equivalent acoustic impedance

The local equivalent acoustic impedance denoted by z^{loc} is defined by

$$p(\tilde{\mathbf{x}}, \omega) = z^{loc}(\tilde{\mathbf{x}}, \omega)\,(v^{P_1}(\tilde{\mathbf{x}}, \omega) - v^{P_2}(\tilde{\mathbf{x}}, \omega)), \quad \forall \tilde{\mathbf{x}} \in S. \tag{9}$$

Sometimes, such a local equivalent impedance z^{loc} is called the wall acoustic impedance [15,16]. From Eqs. (3) and (9), it can be deduced that the local equivalent acoustic impedance can be written as

$$z(\tilde{\mathbf{x}}, \tilde{\mathbf{x}}', \omega) = z^{loc}(\tilde{\mathbf{x}}, \omega)\,\delta_0(\tilde{\mathbf{x}} - \tilde{\mathbf{x}}'), \tag{10}$$

in which, for all $\tilde{\mathbf{x}}'$ belonging to S, $\delta_0(\tilde{\mathbf{x}} - \tilde{\mathbf{x}}')$ is the Dirac function such as $\int_S \phi(\tilde{\mathbf{x}})\,\delta_0(\tilde{\mathbf{x}} - \tilde{\mathbf{x}}')\,\mathrm{d}S_{\tilde{\mathbf{x}}} = \phi(\tilde{\mathbf{x}}')$. It should be noted that $z^{loc}(\tilde{\mathbf{x}}, \omega)$ differs from $z(\tilde{\mathbf{x}}, \tilde{\mathbf{x}}', \omega)$ by a surface element. Introducing the real and the imaginary parts of the local equivalent acoustic impedance such that $z^{loc}(\tilde{\mathbf{x}}, \omega) = z^{loc}_R(\tilde{\mathbf{x}}, \omega) + \mathrm{i} z^{loc}_I(\tilde{\mathbf{x}}, \omega)$, from Eq. (8), it can be deduced that

$$z^{loc}_R(\tilde{\mathbf{x}}, -\omega) = z^{loc}_R(\tilde{\mathbf{x}}, \omega), \quad z^{loc}_I(\tilde{\mathbf{x}}, -\omega) = -z^{loc}_I(\tilde{\mathbf{x}}, \omega). \tag{11}$$

For all $\tilde{\mathbf{x}}$ in S, the local equivalent acoustic impedance has to satisfy the following properties (see Ref. [15]):

$$\begin{aligned} & z^{loc}_R(\tilde{\mathbf{x}}, \omega) > 0, \quad \forall \omega \in \mathbb{R}, \\ & -\omega\, z^{loc}_I(\tilde{\mathbf{x}}, \omega) \geqslant 0, \quad \forall \omega \in [-\omega_0, \omega_0] \quad \text{in which } \omega_0 > 0, \\ & \lim_{\omega \to 0} (-\omega\, z^{loc}_I(\tilde{\mathbf{x}}, \omega)) = \alpha(\tilde{\mathbf{x}}) \geqslant \alpha_{min} > 0, \end{aligned} \tag{12}$$

in which α_{min} is a given real positive constant and $\tilde{\mathbf{x}} \mapsto \alpha(\tilde{\mathbf{x}})$ is a positive-valued function defined on S. Eq. (12) means that $z^{loc}_I(\tilde{\mathbf{x}}, \omega) \sim -\alpha(\tilde{\mathbf{x}})/\omega$ if $\omega \to 0$. For all $\tilde{\mathbf{x}}$ in S, the function $\omega \mapsto z^{loc}_R(\tilde{\mathbf{x}}, \omega)$ is a continuous function and one has

$$\lim_{\omega \to 0} (\omega\, z^{loc}_R(\tilde{\mathbf{x}}, \omega)) = 0. \tag{13}$$

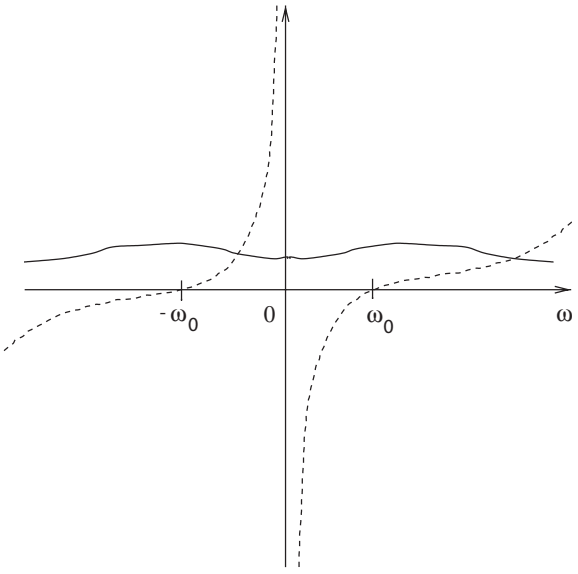

Fig. 6. Acoustic impedance resistance z_R^{loc} (solid line) and acoustic impedance reactance z_I^{loc} (dashed line) for a local equivalent acoustic impedance z^{loc} as a function of frequency ω .

From Eqs. (12) and (13), one deduces that

$$z^{loc}(\tilde{\mathbf{x}},\omega)\neq 0, \quad \forall \tilde{\mathbf{x}}\in S, \quad \forall \omega, \tag{14}$$

$$\{\mathrm{i}\omega\, z^{loc}(\tilde{\mathbf{x}},\omega)\}_{\omega=0} = \{-\omega\, z_I^{loc}(\tilde{\mathbf{x}},\omega)\}_{\omega=0} = \alpha(\tilde{\mathbf{x}}) > 0. \tag{15}$$

The real part corresponds to the dissipative part of $z^{loc}(\tilde{\mathbf{x}},\omega)$ (acoustic impedance resistance). The imaginary part corresponds to the conservative part of $z^{loc}(\tilde{\mathbf{x}},\omega)$ (acoustic impedance reactance). Let $\Delta w(\tilde{\mathbf{x}},\omega) = w^{P_1}(\tilde{\mathbf{x}},\omega) - w^{P_2}(\tilde{\mathbf{x}},\omega)$ be the difference between the normal displacements of the two plates and let be $\Delta v(\tilde{\mathbf{x}},\omega) = v^{P_1}(\tilde{\mathbf{x}},\omega) - v^{P_2}(\tilde{\mathbf{x}},\omega)$. Therefore, one has $\Delta v(\tilde{\mathbf{x}},\omega) = \mathrm{i}\omega\, \Delta w(\tilde{\mathbf{x}},\omega)$. Eq. (9) yields

$$\begin{aligned}\hat{p}(\tilde{\mathbf{x}},\omega) &= z^{loc}(\tilde{\mathbf{x}},\omega)\, \Delta v(\tilde{\mathbf{x}},\omega)\\ &= [-\omega z_I^{loc}(\tilde{\mathbf{x}},\omega) + \mathrm{i}\omega\, z_R^{loc}(\tilde{\mathbf{x}},\omega)]\, \Delta w(\tilde{\mathbf{x}},\omega).\end{aligned} \tag{16}$$

Fig. 6 displays a typical graph (see for instance Ref. [15]) for the functions $\omega \mapsto z_R^{loc}(\tilde{\mathbf{x}},\omega)$ and $\omega \mapsto z_I^{loc}(\tilde{\mathbf{x}},\omega)$.

3.4. Model for the equivalent acoustic impedance density function

Let $\zeta(\tilde{\mathbf{x}},\omega)$ be defined by $\zeta(\tilde{\mathbf{x}},\omega) = z(\tilde{\mathbf{x}},\tilde{\mathbf{x}},\omega)$, and let $\zeta_R(\tilde{\mathbf{x}},\omega)$ and $\zeta_I(\tilde{\mathbf{x}},\omega)$ be the real and the imaginary parts of $\zeta(\tilde{\mathbf{x}},\omega)$ such that $\zeta(\tilde{\mathbf{x}},\omega) = \zeta_R(\tilde{\mathbf{x}},\omega) + \mathrm{i}\zeta_I(\tilde{\mathbf{x}},\omega)$. As explained in Section 3.3, $z^{loc}(\tilde{\mathbf{x}},\omega)$ differs from $\zeta(\tilde{\mathbf{x}},\omega)$ by a surface element. Since $z_R^{loc}(\tilde{\mathbf{x}},\omega) > 0$, one then deduces that $\zeta_R(\tilde{\mathbf{x}},\omega) > 0$. Let $\rho_R(\tilde{\mathbf{x}},\tilde{\mathbf{x}}',\omega)$ be the function corresponding to the normalization of $z_R(\tilde{\mathbf{x}},\tilde{\mathbf{x}}',\omega)$ and

defined by

$$\rho_R(\tilde{\mathbf{x}}, \tilde{\mathbf{x}}', \omega) = \frac{z_R(\tilde{\mathbf{x}}, \tilde{\mathbf{x}}', \omega)}{\sqrt{\zeta_R(\tilde{\mathbf{x}}, \omega)\, \zeta_R(\tilde{\mathbf{x}}', \omega)}}. \tag{17}$$

For the imaginary part, there exists ω_0 such that $\zeta_I(\tilde{\mathbf{x}}, \omega_0) = 0$, for all $\tilde{\mathbf{x}}$. Consequently, the normalization of the imaginary part is defined by

$$\rho_I(\tilde{\mathbf{x}}, \tilde{\mathbf{x}}', \omega) = \frac{z_I(\tilde{\mathbf{x}}, \tilde{\mathbf{x}}', \omega)}{\sqrt{|\zeta(\tilde{\mathbf{x}}, \omega)|\, |\zeta(\tilde{\mathbf{x}}', \omega)|}}. \tag{18}$$

One then obtains

$$z(\tilde{\mathbf{x}}, \tilde{\mathbf{x}}', \omega) = \sqrt{|\zeta(\tilde{\mathbf{x}}, \omega)|\, |\zeta(\tilde{\mathbf{x}}', \omega)|}\, \Bigg(\rho_R(\tilde{\mathbf{x}}, \tilde{\mathbf{x}}', \omega) \times \sqrt{\frac{\zeta_R(\tilde{\mathbf{x}}, \omega)}{|\zeta(\tilde{\mathbf{x}}, \omega)|}}\, \sqrt{\frac{\zeta_R(\tilde{\mathbf{x}}', \omega)}{|\zeta(\tilde{\mathbf{x}}', \omega)|}} + \mathrm{i}\rho_I(\tilde{\mathbf{x}}, \tilde{\mathbf{x}}', \omega) \Bigg). \tag{19}$$

4. Properties of the equivalent acoustic impedance deduced from the experimental analysis

4.1. Experimental analysis

Fig. 7 displays the graph of $\omega \mapsto \mathrm{tr}\{\mathbf{H}^{exp}(\omega)\, \mathbf{H}^{exp}(\omega)^{\bigstar}\}$ with respect to the frequency and shows that frequencies below 300 Hz belong to the low-frequency range (the modal domain), and frequencies above 300 Hz belong to the medium- and high-frequency ranges for which the proposed algebraic model is constructed. When the frequency increases, the experimental equivalent acoustic impedance tends to be a diagonal matrix. For instance, at a frequency 100 Hz,

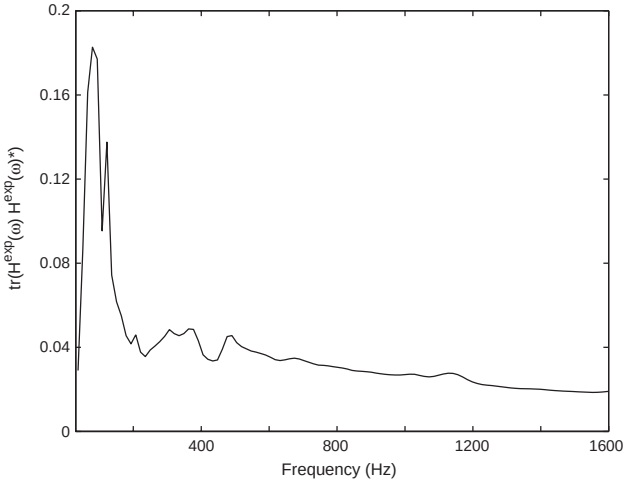

Fig. 7. Graph of $\omega \mapsto \mathrm{tr}\{\mathbf{H}^{exp}(\omega)\mathbf{H}^{exp}(\omega)^{\bigstar}\}$ with respect to the frequency.

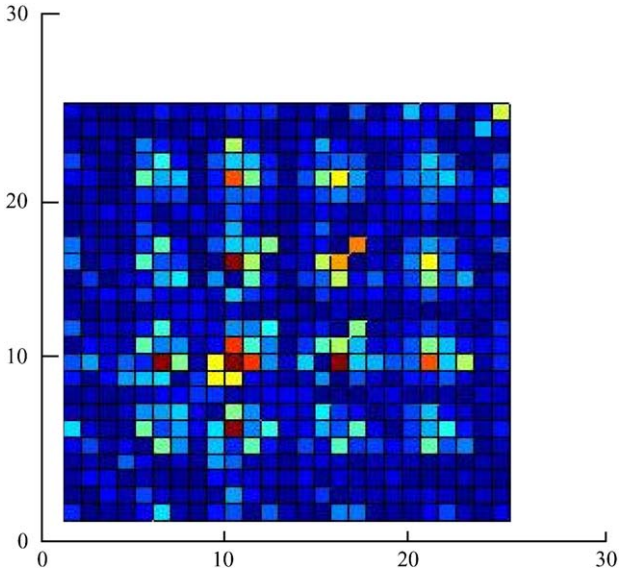

Fig. 8. Real part of the experimental impedance matrix $[\mathbf{Z}^{exp}(2\pi\nu)]_{ij}$ at frequency $\nu = 100$ Hz as a function of indices i and j. The light grey pixels correspond to the higher values and the dark grey pixels to the lower values.

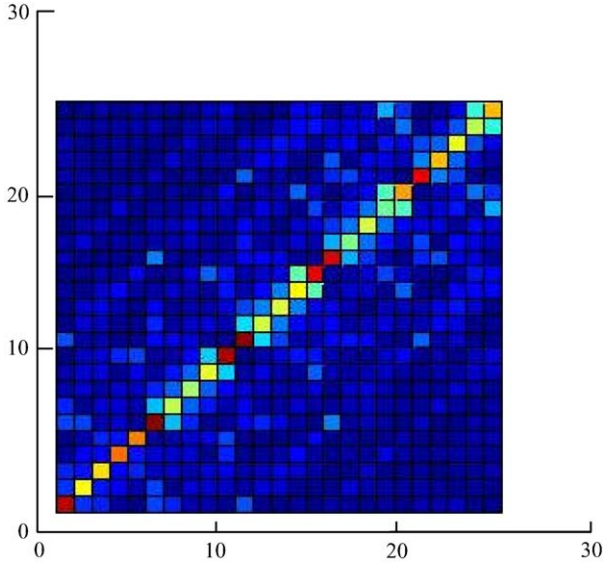

Fig. 9. Real part of the experimental impedance matrix $[\mathbf{Z}^{exp}(2\pi\nu)]_{ij}$ at frequency $\nu = 1200$ Hz as a function of indices i and j. The light grey pixels correspond to the higher values and the dark grey pixels to the lower values.

Fig. 8 shows that the impedance matrix is not diagonal at all. Such a matrix corresponds to an equivalent acoustic impedance which is non-local in space. Conversely, at a frequency of 1200 Hz, this impedance matrix is a quasi-diagonal matrix which means that the equivalent acoustic impedance is almost local in space (see Fig. 9). The detailed analysis of the experimental data basis

shows that the upper bound of the frequency for which the equivalent acoustic impedance is non-local in space is about 300 Hz (this is also the lower bound for which the impedance is almost local in space). An additional detailed analysis of the experimental data basis [13] shows that the experimental equivalent acoustic impedance can be considered as homogeneous and isotropic with respect to the co-ordinates x_1 and x_2 for frequencies greater than 300 Hz. This kind of analysis is too long and cannot be developed here. It should be noted that at high frequencies, Fig. 9 shows that the structure of the impedance matrix is quasi-diagonal which is coherent with the physical point of view. Some small differences appear, especially around the points 1 and 25 which are furthest away from each other relative to the symmetric point 13. These minor differences (not greater than 5–8 Pa s/m) are certainly due to experimental errors (especially, one reason could be that the experimental lateral boundary conditions could induce some differences from one lateral side to another).

4.2. Basic algebraic model

For frequencies greater than 300 Hz, the equivalent acoustic impedance density function is then considered as homogeneous and isotropic. Therefore, the density function $z(\tilde{\mathbf{x}}, \tilde{\mathbf{x}}', \omega)$ depends only on $\|\tilde{\mathbf{x}} - \tilde{\mathbf{x}}'\|$ and is then rewritten as $z(\|\tilde{\mathbf{x}} - \tilde{\mathbf{x}}'\|, \omega)$. Consequently, $\zeta(\tilde{\mathbf{x}}, \omega)$ does not depend on $\tilde{\mathbf{x}}$ and is rewritten as

$$\zeta(\tilde{\mathbf{x}}, \omega) = \zeta(\omega), \quad \zeta(\omega) = \zeta_R(\omega) + \mathrm{i}\zeta_I(\omega). \tag{20}$$

Eq. (19) is then rewritten as

$$z(\|\tilde{\mathbf{x}} - \tilde{\mathbf{x}}'\|, \omega) = |\zeta(\omega)| \left(\rho_R(\|\tilde{\mathbf{x}} - \tilde{\mathbf{x}}'\|, \omega) \frac{\zeta_R(\omega)}{|\zeta(\omega)|} + \mathrm{i}\rho_I(\|\tilde{\mathbf{x}} - \tilde{\mathbf{x}}'\|, \omega) \right). \tag{21}$$

The following algebraic models for the functions $\rho_R(\|\tilde{\mathbf{x}} - \tilde{\mathbf{x}}'\|, \omega)$ and $\rho_I(\|\tilde{\mathbf{x}} - \tilde{\mathbf{x}}'\|, \omega)$ are proposed:

$$\rho_R(\|\tilde{\mathbf{x}} - \tilde{\mathbf{x}}'\|, \omega) = \mathrm{e}^{-\|\tilde{\mathbf{x}} - \tilde{\mathbf{x}}'\|/L_R(\omega)} \cos(2\pi\|\tilde{\mathbf{x}} - \tilde{\mathbf{x}}'\|/\lambda_R(\omega)), \tag{22}$$

$$\rho_I(\|\tilde{\mathbf{x}} - \tilde{\mathbf{x}}'\|, \omega) = \mathrm{e}^{-\|\tilde{\mathbf{x}} - \tilde{\mathbf{x}}'\|/L_I(\omega)} \cos(2\pi\|\tilde{\mathbf{x}} - \tilde{\mathbf{x}}'\|/\lambda_I(\omega) + \phi_I(\omega)). \tag{23}$$

These algebraic models result from an analysis of the experimental data basis [13]. It should be noted that the model of the real part depends on the parameter $L_R(\omega)$ which is the length scale controlling the exponential decrease of the amplitude and on the parameter $\lambda_R(\omega)$ controlling the wavelength of the oscillations. The model of the imaginary part depends on similar parameters $L_I(\omega)$ and $\lambda_I(\omega)$ and on an additional parameter $\phi_I(\omega)$ corresponding to a phase. Eqs. (21)–(23) constitute the underlying algebraic model for the construction of the mean model and the random model of the equivalent acoustic impedance. It should be noted that the parameters L_R, λ_R, L_I, λ_I and ϕ_I have been chosen as a function of ω, and consequently, $\rho_R(\|\tilde{\mathbf{x}} - \tilde{\mathbf{x}}'\|, \omega)$ and $\rho_I(\|\tilde{\mathbf{x}} - \tilde{\mathbf{x}}'\|, \omega)$ defined by Eqs. (22) and (23) dependent on ω. Nevertheless, one will see in the next sections that the values of these parameters will be chosen as quantities independent of ω. This assumption results from a compromise between the simplicity of the model and its capability to represent the experimental data basis. A more sophisticated mean algebraic model could be introduced in choosing these parameters as a function of the frequency. Such a solution has been studied in Ref. [13] and the gain obtained is not significant with respect to the frequency-independent assumption retained for the mean model.

5. Estimating the mean values of the basic algebraic model parameters using the experimental data basis

The objective is to estimate (1) the values of $\zeta_R(\omega)$, $\zeta_I(\omega)$ and $|\zeta(\omega)|$ and (2) the parameters $\underline{L}_R$, $\underline{\lambda}_R$, $\underline{L}_I$, $\underline{\lambda}_I$ and $\underline{\phi}_I$ of the mean algebraic model.

5.1. Construction of a representation of $\zeta_R(\omega)$

Since the experimental values of $\zeta_R^{exp}(\tilde{\mathbf{x}}_j, \omega)$ in the 25 measured points $\tilde{\mathbf{x}}_1, \ldots, \tilde{\mathbf{x}}_{25}$ are close together (which is coherent with the introduced homogeneity assumption), an estimation of $\zeta_R^{exp}(\omega)$ is given by $\zeta_R^{exp}(\omega) = \frac{1}{25}\sum_{j=1}^{25} \zeta_R(\tilde{\mathbf{x}}_j, \omega)$ which represents the experimental mean value. The following algebraic model for $\zeta_R(\omega)$ is proposed:

$$\zeta_R(\omega) = \zeta_{R\,0} + (\zeta_{R\,max} - \zeta_{R\,0})\left(\frac{|\omega|}{\omega_{R0}}\right)^{\gamma_R} \mathrm{e}^{-a_R||\omega|/\omega_{R0}-1|^{b_R}}, \tag{24}$$

in which the parameters $\zeta_{R\,0}$, $\zeta_{R\,max}$, ω_{R0}, γ_R, a_R and b_R are fitted in minimizing $\int_{\mathscr{B}} |\zeta_R^{exp}(\omega) - \zeta_R^{exp}(\omega)|^2 \, \mathrm{d}\omega$ in which $\mathscr{B}$ is the frequency band of analysis. The result of this minimization yields

$$\zeta_{R\,0} = 1.678 \times 10^6 \text{ Pa s m}^{-3}, \quad \zeta_{R\,max} = 4.717 \times 10^6 \text{ Pa s m}^{-3}, \quad \omega_{R0} = 5303 \text{ rad s}^{-1},$$

$$\gamma_R = 2, \quad a_R = 46, \quad b_R = 2.$$

The frequency band of analysis $\mathscr{B}$ is equal to [100,1600] Hz. Fig. 10 displays the graph of $\zeta_R^{exp}(\omega)$ and $\zeta_R(\omega)$ over the frequency band $\mathscr{B}$. The comparison is good.

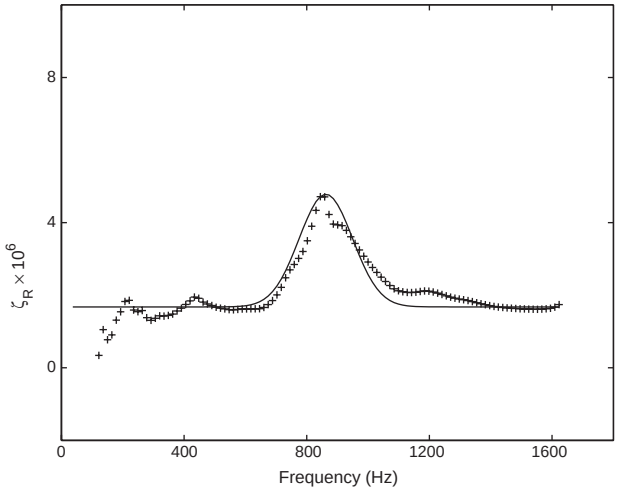

Fig. 10. Graphs of $\zeta_R(\omega)$ (solid line) and of $\zeta_R^{exp}(\omega)$ (cross symbols) over the frequency band [100, 1600] Hz.

5.2. Construction of a representation of $\zeta_I(\omega)$

Similar to the real part case, an estimation of $\zeta_I^{exp}(\omega)$ is returned as

$$\zeta_I^{exp}(\omega) = \frac{1}{25}\sum_{j=1}^{25} \zeta_I(\tilde{\mathbf{x}}_j, \omega)$$

which represents the experimental mean value. The following algebraic model for $\zeta_I(\omega)$ is proposed:

$$\zeta_I(\omega) = \frac{a_I}{\omega}\left(b_I\omega^4 + c_I\,\omega^2 - 1 + \frac{d_I}{(\omega^2 - \omega_{I0}^2)^2 + e_I\omega^2}\right), \tag{25}$$

in which the parameters ω_{I0}, a_I, b_I, c_I, d_I and e_I are fitted in minimizing $\int_{\mathscr{B}} |\zeta_I^{exp}(\omega) - \zeta_I^{exp}(\omega)|^2\,\mathrm{d}\omega$. The result of this minimization yields

$$\omega_{I0} = 4.86 \times 10^3 \text{ rad s}^{-1}, \quad a_I = 4.7 \times 10^9, \quad b_I = 8 \times 10^{-16},$$

$$c_I = 1 \times 10^{-25}, \quad d_I = 1.6 \times 10^{14}, \quad e_I = 2.4 \times 10^6.$$

Fig. 11 displays the graph of $\zeta_I^{exp}(\omega)$ and $\zeta_I(\omega)$ over the frequency band $\mathscr{B}$. The comparison is good.

5.3. Calculation of the modulus $|\zeta(\omega)|$ and experimental comparisons

Fig. 12 shows the comparison of $|\zeta^{exp}(\omega)|$ with $|\zeta(\omega)|$ over the frequency band [100,1600] Hz, the moduli $|\zeta^{exp}(\omega)|$ and $|\zeta(\omega)|$ being calculated using the fitted representation of $\zeta_R(\omega)$ and $\zeta_I(\omega)$.

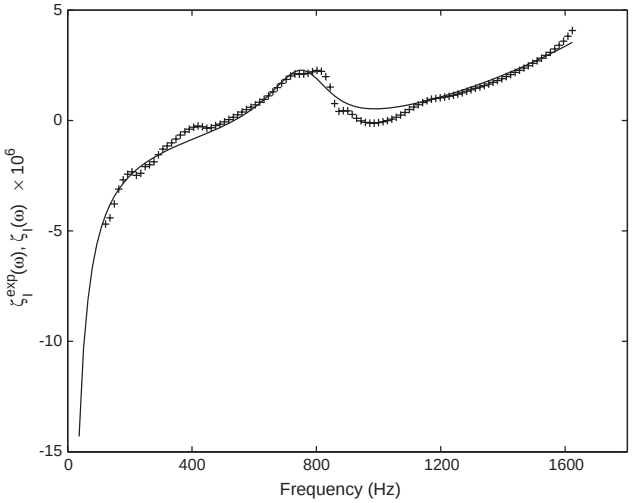

Fig. 11. Graphs of $\zeta_I(\omega)$ (solid line) and of $\zeta_I^{exp}(\omega)$ (cross symbols) over the frequency band [100, 1600] Hz.

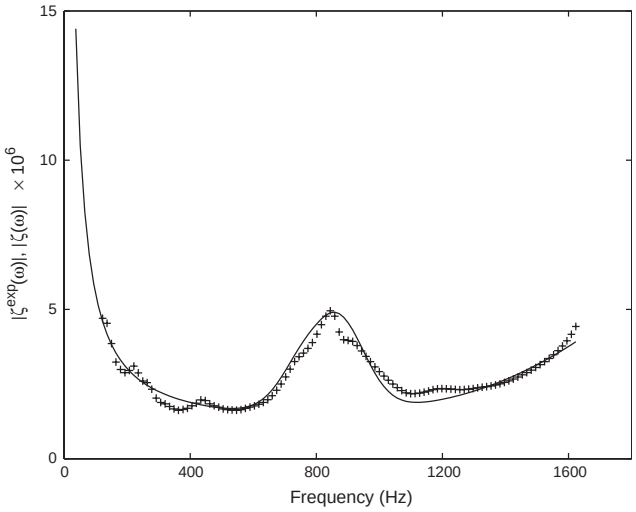

Fig. 12. Graphs of $|\zeta(\omega)|$ (solid line) and of $|\zeta^{exp}(\omega)|$ (cross symbols) over the frequency band $[100, 1600]$ Hz.

5.4. Calculation of the phase and experimental comparisons

Let $\phi_I(\omega)$ be the phase defined by

$$\cos(\phi_I(\omega)) = \frac{\zeta_I(\omega)}{|\zeta(\omega)|}, \quad \psi_I(\omega) \in [0, \pi]. \tag{26}$$

The corresponding experimental value is such that $\cos(\phi_I^{exp}(\omega)) = \zeta_I^{exp}(\omega)/|\zeta^{exp}(\omega)|$. Fig. 13 shows the comparison of $\phi_I^{exp}(\omega)$ with $\phi_I(\omega)$ over the frequency band [100,1600] Hz. It should be noted that in Eq. (23), the mean value $\underline{\phi}_I$ of the phase is then defined as a constant independent of ω, by

$$\underline{\phi}_I = \frac{1}{|\mathscr{B}|} \int_{\mathscr{B}} \phi_I(\omega)\, \mathrm{d}\omega. \tag{27}$$

From the experimental data basis, one obtains $\underline{\phi}_I = 1.1697$ rad.

5.5. Fitting the mean algebraic model

With respect to the real part, the mean algebraic model for ρ_R is defined by

$$\rho_R(\|\tilde{\mathbf{x}} - \tilde{\mathbf{x}}'\|) = \mathrm{e}^{-\|\tilde{\mathbf{x}} - \tilde{\mathbf{x}}'\|/\underline{L}_R} \cos(2\pi \|\tilde{\mathbf{x}} - \tilde{\mathbf{x}}'\|/\underline{\lambda}_R), \tag{28}$$

in which $\eta = \|\tilde{\mathbf{x}} - \tilde{\mathbf{x}}'\|$. In the first step, the mean experimental function

$$\underline{\rho}_R^{exp}(\eta) = \frac{1}{|\mathscr{B}|} \int_{\mathscr{B}} \rho_R^{exp}(\eta, \omega)\, \mathrm{d}\omega$$

is introduced. This function is then deduced from the experimental data basis for the different distances $\eta_1, \eta_2, \ldots$ relative to the driving and receiving points. In the second step, the values $\underline{L}_R$ and $\underline{\lambda}_R$ are calculated in minimizing $\sum_j |\underline{\rho}_R(\eta_j) - \underline{\rho}_R^{exp}(\eta_j)|^2$.

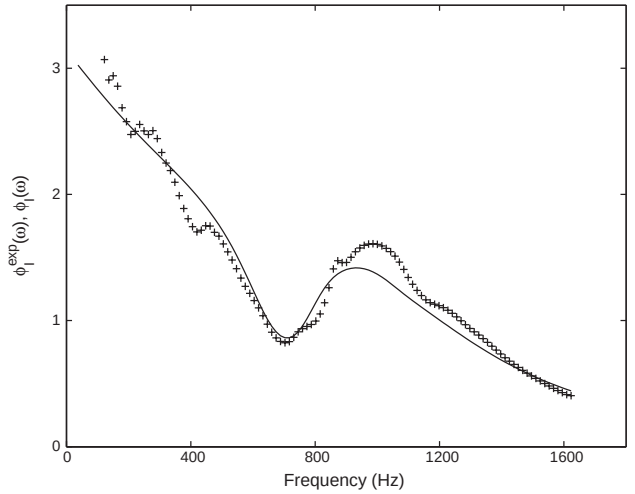

Fig. 13. Graphs of $\phi_I(\omega)$ (solid line) and $\phi_I^{exp}(\omega)$ (cross symbols) over the frequency band $[100, 1600]$ Hz.

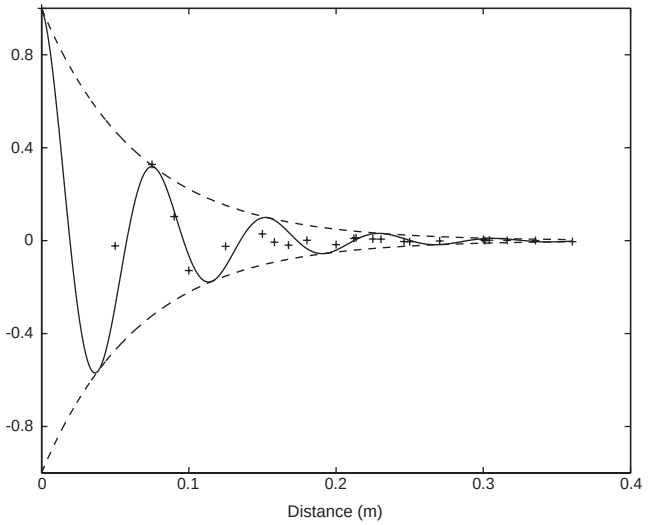

Fig. 14. Graph of the function $\eta \mapsto \varrho_R(\eta)$ (solid line) with $\eta = \|\tilde{\mathbf{x}} - \tilde{\mathbf{x}}'\|$ and graph of its envelope (dashed line). Graph of the function $\eta \mapsto \varrho_R^{exp}(\eta)$ (cross symbols).

One obtains

$$\underline{L}_R = 0.0664, \quad \lambda_R = 0.0771. \tag{29}$$

Fig. 14 shows the graphs of $\eta \mapsto \varrho_R^{exp}(\eta)$ and $\eta \mapsto \varrho_R(\eta)$. Fig. 15 displays the graphs of the functions $\omega \mapsto \rho_R^{exp}(\eta, \omega)$ for all the receiving points having the same distance $\eta = 0.075$ m and the corresponding graph of the function $\omega \mapsto \varrho_R(\eta)$. This figure shows that the frequency averaging introduced is well adapted to the present case and justifies the frequency-independent parameters

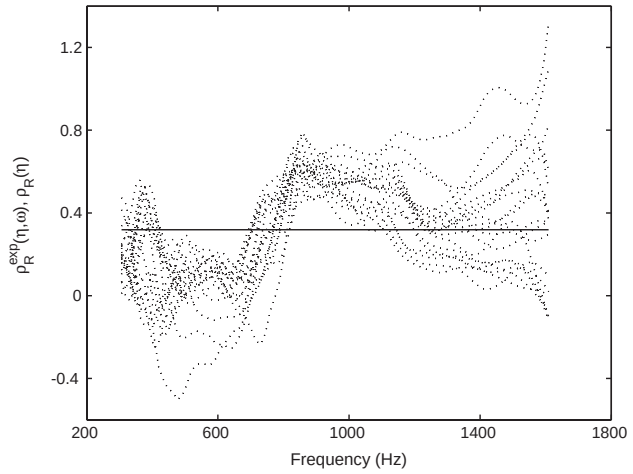

Fig. 15. Graphs of the function $\omega \mapsto \rho_R^{exp}(\eta, \omega)$ (dotted lines) and graph of the function $\omega \mapsto \varrho_R(\eta)$ (solid line) for $\eta = 0.075$ m.

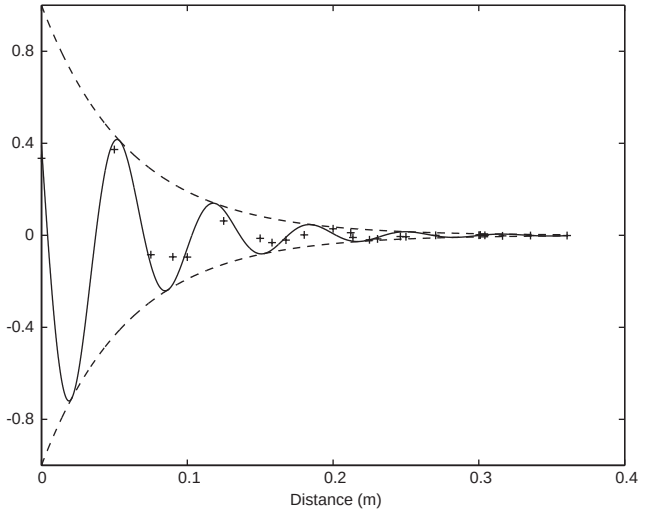

Fig. 16. Graph of the function $\eta \mapsto \varrho_I(\eta)$ (solid line) with $\eta = \|\tilde{\mathbf{x}} - \tilde{\mathbf{x}}'\|$ and graph of its envelope (dashed line). Graph of the function $\eta \mapsto \varrho_I^{exp}(\eta)$ (cross symbols).

assumption. With respect to the imaginary part, the mean model for ρ_I is defined by

$$\rho_I(\eta) = \mathrm{e}^{-\eta/\underline{L}_I} \cos(2\pi\eta/\underline{\lambda}_I + \underline{\phi}_I). \tag{30}$$

Similarly, one introduces the mean experimental function

$$\varrho_I^{exp}(\eta) = \frac{1}{|\mathscr{B}|} \int_{\mathscr{B}} \rho_I^{exp}(\eta, \omega)\, \mathrm{d}\omega$$

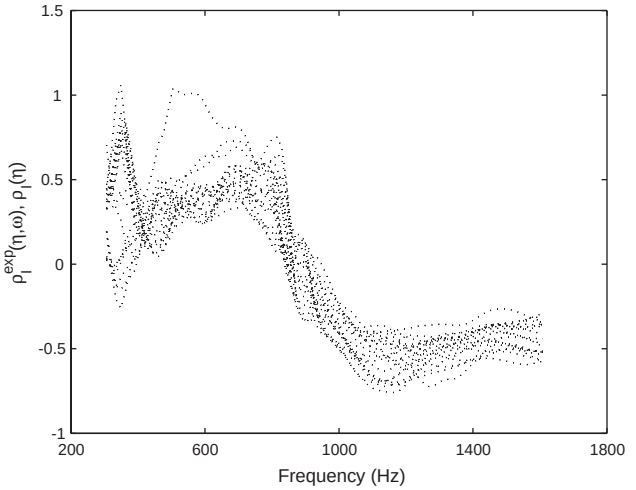

Fig. 17. Graphs of the function $\omega \mapsto \rho_I^{exp}(\eta, \omega)$ (dotted lines) and graph of the function $\omega \mapsto \varrho_I(\eta)$ (solid line) for $\eta = 0.075$ m.

which is deduced from the experimental data basis for the different distances $\eta_1, \eta_2, \ldots$. Then, since $\underline{\phi}_I = 1.1697$ rad, the values $\underline{L}_I$ and $\underline{\lambda}_I$ of the mean algebraic model are calculated by minimizing $\sum_j |\varrho_I(\eta_j) - \rho_I^{exp}(\eta_j)|^2$. One obtains

$$\underline{L}_I = 0.0603, \quad \underline{\lambda}_I = 0.0660. \tag{31}$$

Fig. 16 shows the graphs of $\eta \mapsto \rho_I^{exp}(\eta)$ and $\eta \mapsto \varrho_I(\eta)$. Fig. 17 displays the graphs of the functions $\omega \mapsto \rho_I^{exp}(\eta, \omega)$ for all the receiving points having the same distance $\eta = 0.075$ m and the corresponding graph of the function $\omega \mapsto \varrho_I(\eta)$. Similarly, for the real case, Fig. 17 shows that the frequency averaging introduced is well adapted to the present case and justifies the frequency-independent parameters assumption.

6. Construction of a random model for $\boldsymbol{\rho_R(\eta)}$ and $\boldsymbol{\rho_I(\eta)}$

The model relative to the local impedance (diagonal terms of the impedance matrix) leads to a good model fitting of the experimental data. With respect to the off-diagonal terms of the impedance matrix, which are a function of the distance between the different points of the multilayer system, the deterministic model defined by Eqs. (22) and (23) yields a reasonable approximation with a significant dispersion with respect to all experimental points. Then, a stochastic approach is proposed in order to increase the robustness of the algebraic model in its capability to represent all the experimental data. A detailed analysis has been carried out in order to define the parameters of the basic algebraic model which have to be modelled by a random variable. The retained model is the basic algebraic model in which ζ_R and $|\zeta|$ are modelled by the mean values estimated in Sections 5.1 and 5.3, L_R and L_I are modelled by $\underline{L}_R$ and $\underline{L}_I$ estimated in Section 5.5 and where λ_R, λ_I and ϕ_I are modelled by mutually independent random variables Λ_R,

Λ_I and Φ_I, respectively, independent of frequency ω. By construction, the mean values of these three random variables are $\underline{\lambda}_R$, $\underline{\lambda}_I$ and $\underline{\phi}_I$ estimated in Sections 5.4 and 5.5.

6.1. Estimating the probability distributions of the random parameters

The variables Λ_R and Λ_I are positive-valued random variables and Φ_I is a random variable with values in $[0, 2\pi]$. The maximum entropy principle is used to construct the probability distribution [17] for each random variable Λ_R, Λ_I or Φ_I. Below, Λ_r denotes either Λ_R or Λ_I. It is assumed that the probability distribution of the random variable Λ_r is defined by a probability density function $p_{\Lambda_r}(\lambda)$ with respect to $\mathrm{d}\lambda$. For random variable Λ_r, the available information consists of the mean value $m_1^r = E\{\Lambda_r\}$ and of the second order moment $m_2^r = E\{\Lambda_r^2\}$. Consequently, the maximum entropy principle consists in maximizing entropy $\mathscr{S}$ defined by $\mathscr{S}(p_{\Lambda_r}(\lambda)) = -\int_{\mathbb{R}^+} p_{\Lambda_r}(\lambda)\ln(p_{\Lambda_r}(\lambda))\,\mathrm{d}\lambda$ with the constraints defined by the available information and written as

$$\int_{\mathbb{R}_+} \lambda^l\, p_{\Lambda_r}(\lambda)\,\mathrm{d}\lambda = m_l^r, \quad \text{for } l = 0, 1, 2. \tag{32}$$

One then obtains

$$p_{\Lambda_r}(\lambda) = \mathbb{1}_{\mathbb{R}^+}(\lambda)\, C_0^r\, \mathrm{e}^{-\mu_1^r\lambda - \mu_2^r\lambda^2}, \tag{33}$$

in which $C_0^r > 0$, μ_1^r and $\mu_2^r > 0$ have to be chosen such that the constraints be satisfied. One has $m_0^r = 1$. The moment $m_1^r = \underline{\lambda}_r$ has been calculated in Section 5. The second order moment m_2^r is estimated using the experimental data basis and yields $m_2^R = 0.006994$ (resp. $m_2^I = 0.005107$). Consequently, the standard deviation $\sigma_{\Lambda_r} = \sqrt{m_2^r - \underline{\lambda}_r^2}$ is $\sigma_{\Lambda_R} = 0.0324$ (resp. $\sigma_{\Lambda_I} = 0.0274$). One then has to solve the three algebraic equations defined by the three constraints defined by Eq. (32) in which m_0^r, m_1^r and m_2^r are given and where the unknowns are $C_0^r > 0$, μ_1^r and $\mu_2^r > 0$. This calculation yields

$$\begin{aligned} &C_0^R = 0.926 > 0, \quad \mu_1^R = -67.377, \quad \mu_2^R = 442.809 > 0,\\ &C_0^I = 1.012 > 0, \quad \mu_1^I = -81.157, \quad \mu_2^I = 622.792 > 0. \end{aligned} \tag{34}$$

Using the same methodology for random variable Φ_I, the probability density function $p_{\Phi_I}(\phi)$ is written as

$$p_{\Phi_I}(\phi) = \mathbb{1}_{[0,2\pi]}(\phi)\, C_0^\phi\, \mathrm{e}^{-\mu_1^\phi\phi - \mu_2^\phi\phi^2}, \tag{35}$$

in which C_0^ϕ, μ_1^ϕ and μ_2^ϕ have to be such that

$$\int_0^{2\pi} \phi^l\, p_{\Phi_I}(\phi)\,\mathrm{d}\phi = m_l^\phi, \quad l = 0, 1, 2, \tag{36}$$

and where $m_0^\phi = 1, m_1^\phi = \underline{\phi}_I$ has been calculated in Section 5 and where the second order moment m_2^ϕ is estimated with the experimental data basis and yields $m_2^\phi = 1.5085$. Consequently, the standard deviation $\sigma_{\Lambda_\phi} = \sqrt{m_2^\phi - \underline{\phi}_I^2}$ is 0.3745 rad. The calculation of C_0^ϕ, μ_1^ϕ and μ_2^ϕ yields

$$C_0^\phi = 10.776, \quad \mu_1^\phi = 11.124, \quad \mu_2^\phi = -1.623. \tag{37}$$

6.2. Construction of the probabilistic algebraic model for $\rho_R(\eta)$

From the basic algebraic model and from the hypotheses introduced in Section 4.2, the real-valued random variable $\rho_R(\eta)$ is defined by

$$\rho_R(\eta) = \mathrm{e}^{-\eta/\underline{L}_R} \cos(2\pi\eta/\Lambda_R). \tag{38}$$

For a fixed value η of the distance, the confidence region of $\rho_R(\eta)$, corresponding to a given probability level P_c, is defined by the upper envelope $\rho_R^+(\eta)$ and the lower envelope $\rho_R^-(\eta)$ such that

$$\mathscr{P}\{\rho_R^-(\eta) < \rho_R(\eta) < \rho_R^+(\eta)\} \geqslant P_c. \tag{39}$$

The mean value and the second order moment of the random variable $\rho_R(\eta)$ are such that

$$E\{\rho_R(\eta)^\alpha\} = \int_0^{+\infty} p_{\Lambda_R}(\lambda)\, \{\mathrm{e}^{-\eta/\underline{L}_R} \cos(2\pi\eta/\lambda)\}^\alpha \,\mathrm{d}\lambda, \quad \alpha = 1, 2, \tag{40}$$

and the variance is

$$\sigma_{\rho_R}^2(\eta) = E\{\rho_R(\eta)^2\} - (E\{\rho_R(\eta)\})^2. \tag{41}$$

The upper envelope is constructed by using Tchebychev's inequality which, for a real-valued centered random variable X, is written as

$$\mathscr{P}(|X| \geqslant \varepsilon) \leqslant E\{|X|^2\}/\varepsilon^2. \tag{42}$$

One then has

$$\mathscr{P}\{|\rho_R(\eta) - E\{\rho_R(\eta)\}| \geqslant \varepsilon_R(\eta)\} \leqslant E\{|\rho_R(\eta) - E\{\rho_R(\eta)\}|^2\}/\varepsilon_R^2(\eta). \tag{43}$$

Using Eq. (41) yields

$$\mathscr{P}\{|\rho_R(\eta) - E\{\rho_R(\eta)\}| \geqslant \varepsilon_R(\eta)\} \leqslant \sigma_{\rho_R}^2(\eta)/\varepsilon_R^2(\eta), \tag{44}$$

and consequently,

$$\mathscr{P}\{|\rho_R(\eta) - E\{\rho_R(\eta)\}| < \varepsilon_R(\eta)\} \geqslant P_c, \tag{45}$$

in which $P_c = 1 - \sigma_{\rho_R}^2(\eta)/\varepsilon_R^2(\eta)$. The probability level P_c being fixed, one obtains $\varepsilon_R(\eta) = \sigma_{\rho_R}(\eta)/\sqrt{1 - P_c}$. Eq. (45) is rewritten as

$$\mathscr{P}\{-\varepsilon_R(\eta) + E\{\rho_R(\eta)\} < \rho_R(\eta) < \varepsilon_R(\eta) + E\{\rho_R(\eta)\}\} \geqslant P_c. \tag{46}$$

Comparing Eq. (46) with Eq. (39) yields

$$\rho_R^+(\eta) = E\{\rho_R(\eta)\} + \varepsilon_R(\eta), \quad \rho_R^-(\eta) = E\{\rho_R(\eta)\} - \varepsilon_R(\eta). \tag{47}$$

The confidence region corresponding to a probability level equal to 0.95 is shown in Fig. 18. In this figure, each vertical solid line consists of a set of dot symbols corresponding to the experimental values for a same distance η. It should be noted that almost all the significant experimental data are inside the confidence region (95%).

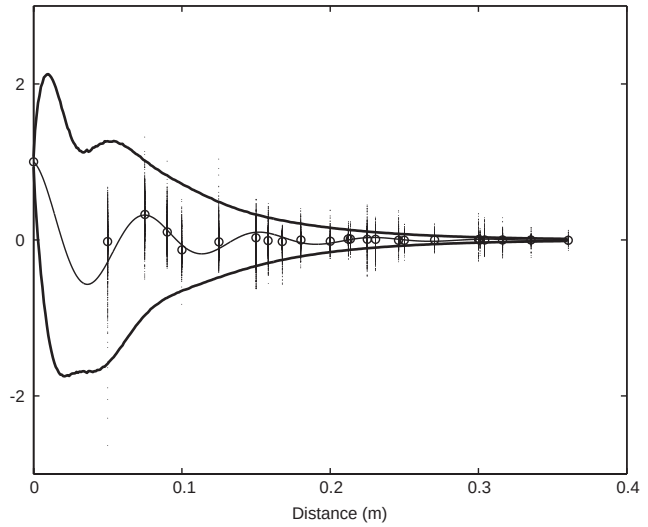

Fig. 18. Confidence region of $\eta \mapsto \varrho_R(\eta)$. Upper envelope $\eta \mapsto \varrho_R^+(\eta)$ (upper thick solid line). Lower envelope $\eta \mapsto \varrho_R^-(\eta)$ (lower thick solid line). Mean algebraic model $\eta \mapsto \varrho_R(\eta)$ (thin solid line). Experimental data (vertical solid line constituted of dot symbols). Mean value of these experimental data (circle symbols).

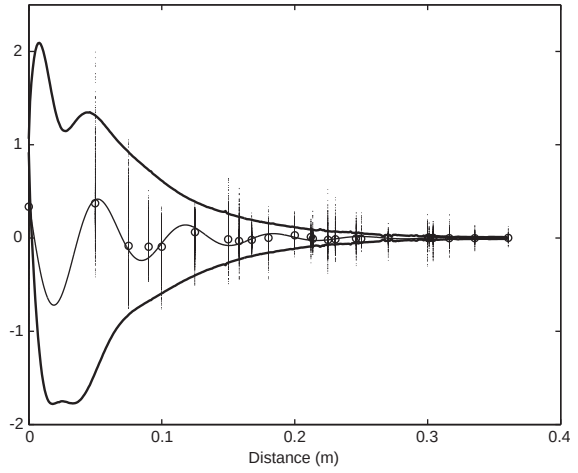

Fig. 19. Confidence region of $\eta \mapsto \varrho_I(\eta)$. Upper envelope $\eta \mapsto \varrho_I^+(\eta)$ (upper thick solid line). Lower envelope $\eta \mapsto \varrho_I^-(\eta)$ (lower thick solid line). Mean algebraic model $\eta \mapsto \varrho_I(\eta)$ (thin solid line). Experimental data (vertical solid line constituted of dot symbols). Mean value of these experimental data (circle symbols).

6.3. Construction of the probabilistic algebraic model for $\rho_I(\eta)$

Using the approach defined in Section 6.2, the real-valued random variable $\rho_I(\eta)$ is defined by

$$\rho_I(\eta) = \mathrm{e}^{-\eta/L_I} \cos(2\pi\eta/\Lambda_I + \Phi_I), \tag{48}$$

which depends on the random variables Λ_I and Φ_I. The confidence region of $\rho_I(\eta)$ is defined by

$$\mathscr{P}(\rho_I^-(\eta) < \rho_I(\eta) < \rho_I^+(\eta)) \geqslant P_c, \tag{49}$$

in which the upper envelope is defined by $\rho_I^+(\eta) = E\{\rho_I(\eta)\} + \varepsilon_I(\eta)$ and the lower envelope is defined by $\rho_I^-(\eta) = E\{\rho_I(\eta)\} - \varepsilon_I(\eta)$ with $\varepsilon_I(\eta) = \sigma_{\rho_I}(\eta)/\sqrt{1-P_c}$. The mean value and the second order moment of the random variable $\rho_I(\eta)$ are defined by

$$E\{\rho_I(\eta)^\alpha\} = \int_0^{+\infty} \int_0^{2\pi} p_{\Lambda_I}(\lambda)\, p_{\Phi_I}(\phi)\, \{e^{-\eta/L_I}\cos(2\pi\eta/\lambda + \phi)\}^\alpha \, d\lambda \, d\phi, \quad \alpha = 1, 2. \tag{50}$$

The variance is such that $\sigma_{\rho_I}^2(\eta) = E\{\rho_I(\eta)^2\} - (E\{\rho_I(\eta)\})^2$. The confidence region corresponding to a probability level equal to 0.95 is shown in Fig. 19. In this figure, each vertical solid line consists of a set of dot symbols corresponding to the experimental values for a same distance η. Similarly for the probabilistic model $\rho_R(\eta)$, it can be shown that almost all the significant experimental data are inside the confidence region (95%).

7. Conclusions

Soundproofing schemes including porous materials are difficult to model. The objective of Part 1 of this paper is to construct an equivalent acoustic impedance for a multilayer system consisting of a three-dimensional porous medium inserted between two thin plates. The construction of a probabilistic algebraic model is based on the introduction of an adapted algebraic model and on the use of an experimental data basis specifically carried out for this research. The probabilistic algebraic model consists of the mean algebraic model and of the probability distribution of the random model parameters. A minimum number of parameters in the model is used and the parameters are fitted using the experimental data basis. The probability distributions are modelled using the entropy maximum principle. This work has been performed in order to construct an algebraic representation which synthesizes a large experimental data basis over the medium- and high-frequency ranges, using a small number of parameters for the algebraic model. The comparison between this model and the experiments is good and consequently, this model can be considered as a synthesis of this experimental data basis and will be reused for other researches.

Acknowledgements

The authors would like to thank ONERA which supports this research.

Appendix A. Geometry and materials properties of the experimental multilayer system

The multilayer system consists of a porous medium and of two plates in alumini for which their thicknesses are $h_{P_1} = 1$ mm and $h_{P_2} = 3$ mm. Table 1 summarizes the plate parameters. The porous medium is a polyurethane foam saturated in air whose thickness H is 100 mm. Table 2

Table 1
Physical parameters for plates P_1 and P_2

Parameters	Value
Young's modulus	$E^P = 7.4 \times 10^{10}$ Pa
Poisson's ratio	$\nu^P = 0.33$
Structural damping factor	$\eta^P = \omega a_1^P(\omega) = 10^{-4}$
Mass density	$\rho^P = 2800$ kg m^{-3}

Table 2
Physical parameters for air into the porous medium

Parameters	Value
Mass density	$\rho_f = 1.213$ kg m^{-3}
Adiabatic bulk modulus	$K_a = 1.42 \times 10^5$ Pa
Viscosity	$\eta_f = 1.84 \times 10^{-5}$ kg m^{-1}s^{-1}
Prandtl number	$Pr = 0.71$
Specific heats ratio	$\gamma = 1.4$

Table 3
Solid phase parameters and fluid–solid coupling parameters for the porous medium

Parameters	Value
Mass density of the solid phase	$\rho_1 = 34.2$ kg m^{-3}
Young's modulus	$E = 110,000$ Pa
Transverse modulus	$G = 40,741$ Pa
Structural damping factor	$\eta_s = \omega a_1(\omega) = 0.09$
Poisson's ratio	$\nu = 0.35$
Porosity	$\Phi = 0.96$
Tortuosity	$\alpha = 1.27$
Resistivity	$\sigma = 10,867$ N s m^{-4}
Viscous characteristic length	$\Lambda = 96$ μm
Thermal characteristic length	$\Lambda' = 288$ μm

summarizes the air parameters. The parameters of the porous medium, introduced in the Biot theory applied in the acoustic problems and characterizing the solid phase and the fluid–solid coupling, have been measured [12,18]. A summary of these results is presented in Table 3.

References

[1] J.F. Allard, *Propagation of Sound in Porous Media: Modeling Sound Absorbing Materials*, Chapman & Hall, London, 1993.

[2] J.F. Allard, A. Aknine, C. Depollier, Acoustical properties of partially reticulated foams with high and medium flow resistance, *Journal of the Acoustical Society of America* 79 (6) (1986) 1734–1740.
[3] J.F. Allard, Y. Champoux, C. Depollier, Modelization of layered sound absorbing materials with transfert matrices, *Journal of the Acoustical Society of America* 82 (5) (1987) 1792–1796.
[4] W. Lauriks, A. Cops, J.F. Allard, C. Depollier, P. Rebillard, Modelization at oblique incidence of layered porous materials with impervious screens, *Journal of the Acoustical Society of America* 87 (3) (1990) 1200–1206.
[5] W. Lauriks, P. Mees, J.F. Allard, The acoustic transmission through layered systems, *Journal of Sound and Vibration* 155 (1) (1992) 125–132.
[6] J.S. Bolton, N.M. Shiau, Y.J. Kang, Sound transmission through multi-panel structures lined with elastic porous materials, *Journal of Sound and Vibration* 191 (3) (1996) 317–347.
[7] J.S. Bolton, N.M. Shiau, Random incidence transmission loss of lined finite double panel systems, *AIAA 12th Aeroacoustics Conference*, San Antonio, October 1989, Paper AIAA-89-1048.
[8] B.H. Song, J.S. Bolton, A transfer-matrix approach for estimating the characteristic impedance and wave numbers of limp and rigid porous materials, *Journal of the Acoustical Society of America* 107 (3) (2000) 1131–1152.
[9] A. Trochidis, A. Kalatouris, Sound transmission through double partitions with cavity absorption, *Journal of Sound and Vibration* 107 (2) (1986) 321–327.
[10] J.A. Moore, R.H. Lyon, Sound transmission loss characteristics of sandwich panel constructions, *Journal of the Acoustical Society of America* 89 (2) (1991) 777–791.
[11] B. Faverjon, C. Soize, Equivalent acoustic impedance model. Part 2: analytical approximation, *Journal of Sound and Vibration* 276 (3–5) (2004) 593–613, this issue.
[12] L. Guillaumie, Wall acoustic impedance, Experimental identification, ONERA Report, No. RTS 2/03239 DDSS, 2001 (in French).
[13] B. Faverjon, Modélisation et Validation Expérimentale d'un Modèle d'Impédance Acoustique dans le Domaine des Moyennes et Hautes Fréquences pour un Système Multicouche Composé d'un Matériau Poreux Épais Inséré entre Deux Plaques Minces, Thèse de Doctorat, Conservatoire National des Arts et Métiers, 2002.
[14] B. Faverjon, C. Soize, Algebraic model of a wall acoustic impedance constructed using experimental data, *Proceedings of the International Conference on Noise and Vibration Engineering*, Leuven, September 2002, pp. 2123–2132.
[15] R. Ohayon, C. Soize, *Structural Acoustics and Vibration*, Academic Press, San Diego, 1998.
[16] A.D. Pierce, *Acoustics*: *An Introduction to its Physical Principles and Applications*, McGrawHill, New York, 1981, re-issued Acoustical Society of America Publications on Acoustics, New York, 1989.
[17] J.N. Kapur, H.K. Kesavan, *Entropy Optimization Principles with Applications*, Academic Press, San Diego, 1992.
[18] N. Dauchez, Characterization of a poroelastic material, CTTM—ONERA Report, 2001 (in French).